Published in *J. Low Temp. Phys.* **156**, 95-115 (2009).

Journal of Low Temperature Physics manuscript No.
(will be inserted by the editor)

V. B. Efimov[1,2], **A. N. Ganshin**[1],
G. V. Kolmakov[2,3], **P. V. E. McClintock**[1],
and L. P. Mezhov-Deglin[2]

Acoustic Turbulence in Superfluid ^{4}He

May 26, 2009

Keywords Wave turbulence, superfluid ^{4}He, second sound, energy cascade
Abstract Recent work on nonlinear second sound wave propagation and acoustic turbulence in superfluid ^{4}He is reviewed. Observations of direct and inverse turbulent energy cascades are described. The direct cascade arises due to the huge nonlinear dependence of the second sound wave velocity on its amplitude. The flux of energy injected at the driving frequency is transformed via successively higher harmonics until it is eventually attenuated by viscous dissipation at the short wavelength edge of spectrum. The onset of the inverse cascade occurs above a critical driving energy density, and it is accompanied by giant waves that constitute an acoustic analogue of the rogue waves that occasionally appear on the surface of the ocean. The theory of the phenomena is outlined and shown to be in good agreement with the experiments.

PACS Numbers: 67.40.Pm; 67.60.Fp.

1 INTRODUCTION

Turbulence implies a highly excited state of a system with numerous degrees of freedom, usually characterized by a directional energy flux through frequency scales[1,2]. The phenomenon arises in a number of variants and in a range of different contexts but, typically, energy is continuously fed into the system on one length scale (or frequency), cascades through the frequency scales without significant dissipation, and is finally dissipated on a smaller length scale (or higher frequency). It is an inherently nonequilibrium phenomenon in the sense that, if

1:Department of Physics, Lancaster University, Lancaster, LA1 4YB, UK

2:Institute of Solid State Physics RAS, 142432, Chernogolovka, Russia

3:Currently at the Department of Chemical and Petroleum Engineering,
Pittsburgh University, Pittsburgh, PA 15261, USA

the driving force is removed, the turbulence dies away and disappears. Different kinds of turbulent behavior may be distinguished by the physical processes providing the energy pumping and energy transformation. In this sense we can usefully distinguish between hydrodynamic, convectional, and wave turbulence. They all are described by nonlinear equations, but their driving and inertial forces are different in nature. Although there are differing reasons for the instabilities in the motion, and differing mechanisms of energy transformation, the dissipative process is always the viscosity of the medium.

Hydrodynamic turbulence appears in a moving fluid when the inertial effects of its motion dominate substantially over viscous forces, i.e. when the Reynolds number Re is large. In the familiar scenario of 2D fluid flow around an obstacle (e.g. in a river), hydrodynamic turbulence appears as individual vortices, and evolves via a Karman vortex street towards fully developed turbulence[3,4]. Convective turbulence appears for steady heating of a liquid in a gravitational field, when the ratio between the Archimedean and viscous forces becomes large, i.e. when the Rayleigh number Ra is large. With increasing Ra there is a transformation from a thermal conductivity regime towards fully developed turbulence via regular flux structures like Rayleigh-Bénard cells and axisymmetric vortex flow[5].

Quantum turbulence (QT) in He II is an example of hydrodynamic turbulence, but with the important difference that the circulation around the vortex cores is singly-quantized, so that all elements of vortex are identical. Our current understanding[6,7] of QT in He II postulates a two-stage decay of turbulent energy initially in the form of quantized vortex lines of relatively large characteristic length. First there is a Richardson cascade towards vortex lines of smaller length scale, leading to the generation of Kelvin waves on the lines. Secondly, there is an analogous turbulent decay of the Kelvin waves until their wavelength is short enough that direct phonon generation becomes probable, finally dissipating the turbulent energy in the form of heat. This Kelvin wave decay is an example of wave turbulence (WT).

Our present paper treats another example of pure WT in He II, in the absence of vortices. We consider second sound WT, a form of acoustic turbulence that offers particular advantages in terms of experimental characterization and control, as we shall see below. Note that acoustic WT is also known to arise in e.g. phonon turbulence in solids[8], turbulence of sound waves in oceanic waveguides[9], magnetic turbulence in interstellar gases[10], and shock waves in the solar wind and their coupling with Earth's magnetosphere[11]. In all cases there is a cascade-like transfer of turbulent energy towards the high frequency domain[2,12], which is where the viscous dissipation mainly occurs.

In what follows, we review recent experimental investigations of acoustic WT created in a system of second sound standing waves in a high-quality resonator filled with He II. Second sound (temperature/entropy) waves are a macroscopic quantum effect seen in superfluids and highly anharmonic crystals.[13,14,15,16] The properties of second sound in He II have been extensively investigated in earlier studies, both experimentally and theoretically. More recently, attention has been focused on the nonlinear acoustic properties of He II.[17,18,19,20,21] These lead[13,14,21,22] to the formation of a planar or spherical shock wave[23,24,25] (temperature discontinuity) during the propagation of a finite-amplitude heat pulse in He II, at short distances from the source (heater). The velocity u_2 of a traveling

second sound wave depends on its amplitude and, to a first approximation, can be written as

$$u_2 = u_{20}\,(1+\alpha\delta T)\,, \tag{1}$$

where δT is the wave amplitude, u_{20} is the velocity of a wave of infinitely small amplitude, and α is the nonlinearity coeffcient of second sound, which is determined by the relation [14]

$$\alpha = \frac{\partial}{\partial T}\ln\left(u_{20}^3\frac{C}{T}\right),$$

C is the heat capacity per unit mass of liquid helium at constant pressure, and T is the temperature.

The nonlinearity coefficient α may be either positive or negative, depending on the temperature and pressure. [14,22,26] Under the saturated vapor pressure (SVP), in the region of roton second sound (i.e. at $T > 0.9$ K) the nonlinearity coefficient is positive ($\alpha > 0$) at temperatures $T < T_\alpha = 1.88$ K (like the nonlinearity coefficient of conventional sound waves in ordinary media), but it is negative ($\alpha < 0$) in the range $T_\alpha < T < T_\lambda$. Here $T_\lambda = 2.176$ K is the temperature of the superfluid-to-normal (He-II to He-I) transition. At $T = T_\alpha$ the nonlinearity coefficient passes through zero.

It is when $T \neq T_\alpha$, that the nonlinear evolution leads to the creation of a shock in the profile of a travelling second sound pulse. During the propagation of a plane, one-dimensional wave of heating (compression) of second sound ($\delta T > 0$), the shock appears at the front of the propagating wave for temperatures 1 K $< T <$ T_α, and on the trailing edge of the wave for temperatures $T_\alpha < T < T_\lambda$ (see, for example, Fig. 2 below). The ease with which α can be adjusted (by alteration of T) and the large values it can take make second sound in He II ideal as a test-bed for the study of nonlinear wave interactions and associated phenomena, including WT. The frequency of second sound depends on its wave vector k as [27]

$$\omega = u_{20}k\left[1+\lambda\xi^2k^2+\ldots\right],$$

where $\xi = \xi_0(1-T/T_\lambda)^{-2/3}$, $\xi_0 \sim 2-3$ A, and $\lambda \sim 1$. We emphasize, however, that the dispersion of second sound is only significant within a close vicinity of the superfluid transition (i.e. at $T_\lambda - T < 1$ μK) and is extremely weak in the temperature range $T < 2.1$ K relevant for the present investigations.

Our most recent studies demonstrate that wave energy can flow, not only towards higher frequencies as in the conventional scenario [12], but also in the opposite direction [28], leading to the appearance of waves at lower frequencies. This leads to formation of the acoustic analogue of the oceanic giant waves that sometimes endanger large ships. Realistic experiments on oceanic giant waves are of course almost impossible, because they probably require hundreds of miles of open sea to build up and decay. As we will see, however, second sound provides an excellent modeling medium for studies of the nonlinear wave interactions believed to be involved in the generating mechanism [29], enabling the fundamental ideas to be tested in the laboratory under controlled conditions.

We have found that this flux of energy towards lower frequencies (inverse cascade) can coexist with the direct cascade. The backflow appears to be attributable

to a decay instability, i.e. nonlinear decay of the wave into two waves of lower frequency governed by the conservation law[2]

$$\omega_1 = \omega_2 + \omega_3. \tag{2}$$

where $\omega_i = u_{20}k_i$ is the frequency of a linear wave of wave vector k_i. The instability results in the creation of subharmonics and can produce a substantial increase of low-frequency wave amplitude. A similar parametric process, but caused by 4-wave processes (modulation instability), is thought[29] to be responsible for the conversion of the energy in ordinary wind-driven waves on the ocean to take the form of rogue waves; this mechanism differs from an alternative explanation proposed recently[30] involving the scattering of nonlinear waves on a continuous noisy background. Comparable decay instabilities have been studied for e.g. spin waves[31,32,33], magnetohydrodynamic waves in plasma[34], and interacting first and second sound waves in superfluid helium near the superfluid transition[35].

In Sec. 2 we outline the experimental techniques used for the present investigations. Sec. 3 describes the propagation of single pulses of second sound in He II and how their shapes change as a consequence of the nonlinearity of the medium. In Sec. 4 we present our results on the forward and inverse turbulent energy cascades, and we discuss their implications is Sec. 5. Finally, in Sec. 6, we summarise our conclusions. We emphasise that the research programme is still in progress and that additional significant results are to be anticipated, especially in relation to transient effects and the kinetics of these turbulent phenomena which we only mention briefly, for completeness, in the present review.

2 EXPERIMENTAL TECHNIQUES

The experimental arrangements[36] are shown schematically in Fig. 1. The cryoacoustical resonator was made of a cylindrical quartz tube of nominal length $L = 7$ cm and internal diameter $D = 1.5$ cm, filled with superfluid helium. The low-inertial film heater and bolometer were deposited on the surfaces of flat glass plates capping the ends of the tube. The heater could be driven by a voltage pulse generator in experiments with solitary traveling waves, or by a harmonic voltage generator for experiments with quasi-one-dimensional standing waves.

For the experiments described below, the heater of resistance R was driven by a sinusoidal voltage $U = U_0 \sin \omega t$. The corresponding total heat flux is

$$W_{tot} = \frac{U^2}{R} = \left(\frac{U_0^2}{R}\right) \times \sin^2(\omega t) = \left(\frac{U_0^2}{2R}\right) \times (1 - \cos(2\omega t)) = W_0 + W. \tag{3}$$

It therefore has both constant, W_0, and periodic, W, components. The frequency of the harmonic voltage generator was set within the range 0.1 – 100 kHz so that the second sound frequency (at twice the generator frequency) was close to that of a longitudinal resonance in the cell. The amplitude δT of the resultant standing wave could be varied from 0.05 mK up to a few mK by adjustment of the power to the heater.

The Mach number in the second sound standing wave can reach $\mathrm{M} = |v_n - v_s|/u_{20} \sim 10^{-4} - 10^{-2}$, where v_n and v_s are the normal and superfluid velocities.

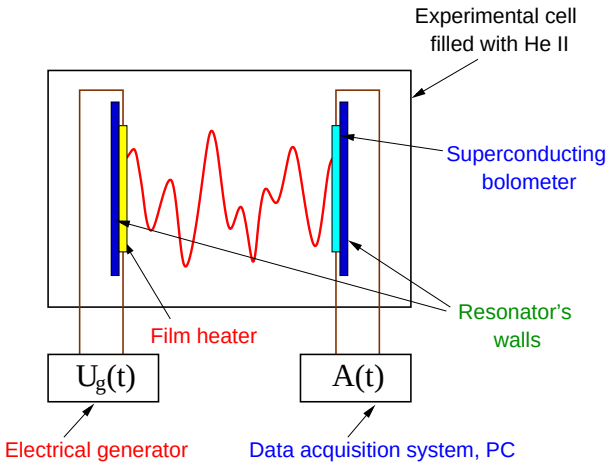

Fig. 1 Schematic diagram illustrating the experimental arrangements. The cylindrical walls of the resonator are not shown.

The proper Reynolds number, defined[37] as

$$\mathrm{Re} = \frac{\alpha u_{20}}{\gamma_\omega}\left(\frac{\partial \delta T}{\partial x}\right) \sim \alpha Q \delta T,$$

can be changed from 1 to 90 (here γ_ω is the damping coefficient of a second sound wave of frequency ω, evaluated from the Q-factor of the resonator). It allows us to study the transition to turbulence in the system of second sound waves as the driving amplitude is increased.

The measured heat flux density W into the liquid is subject to systematic uncertainties of up to $\pm 10\%$ associated with estimation of the resonator cross-section and the resistances of the leads, and possible small inhomogeneities in the heater film thickness. The Q-factor of the resonator determined from the widths of longitudinal resonances at small heat fluxes $W \leq 1$ mW/cm^2 (nearly linear regime) was $Q \sim 3000$ for resonance numbers $20 < p < 100$ and decreased to about 500 at frequencies below 500 Hz ($p < 5$).

The advantage of using a high-Q resonator in this way is that it enables us to create nonlinear second sound standing waves of high amplitude ($\delta T \sim 1$ mK) accompanied by only small heat input at the source $W < 50$ mW/cm^2. We thus avoid possible complications[20,37] due to vortex creation in the bulk He II or nonlinear phenomena at the heater/superfluid interface. The second sound waveform registered by the bolometer was Fourier-analyzed and its power spectrum was computed.

3 PROPAGATION OF NONLINEAR SECOND SOUND PULSES IN He II

Next, we consider briefly the propagation of second sound pulses, and how they are affected by the nonlinearity of the medium (see above). It is the ready adjustability of the nonlinearity coefficient α, and the fact that it can be made very large,

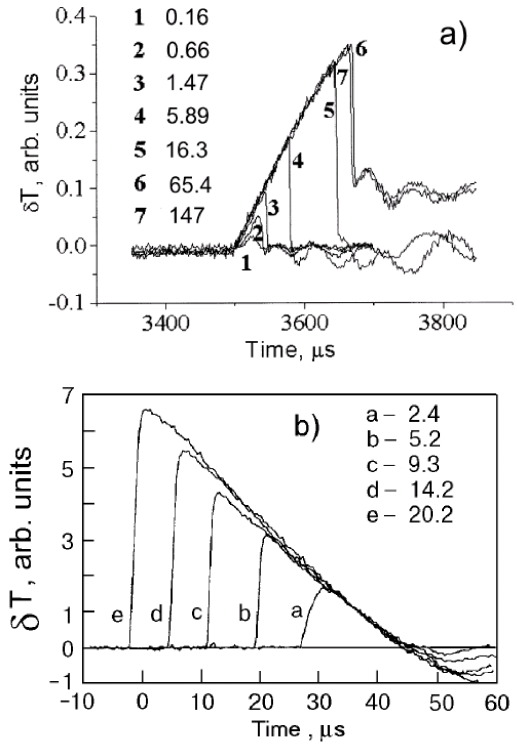

Fig. 2 Evolution in shape of planar second sound waves for increasing heat flux density W from the heater, where δT is the temperature change measured at the bolometer placed at the distance $L = 2.5$ cm from the heater: (a) for a He-II bath temperature of $T = 2.10$ K ($\alpha < 0$), pressure $P = 3$ atm; (b) for $T = 1.50$ K ($\alpha > 0$), pressure $P = P_{SV}$. The numbers beside the curves indicate the heat flux density W expressed in W/cm^2. The time duration of the electrical pulse to the heater was $\tau_e = 10$ μs. Maximal values of the wave amplitude correspond to $\delta T \leq 5$ mK. From Efimov et al.[26]

that make He II uniquely suitable as a model medium for the study of nonlinear wave interactions and wave turbulence under well-controlled conditions.

Fig. 2(a) shows the evolution with heat flux density in the shapes of planar second sound pulses excited by a rectangular heat pulse[26] at temperature $T =$ 2.10 K, pressure $P = 3$ atm., conditions for which $\alpha < 0$. The duration of the electrical pulse applied to the resistive heater was $\tau_e = 10$ μs. The numbers beside the curves correspond to different heat flux densities W from the heater. It is clearly evident in that a shock wave is formed on the trailing edge of the pulse. Creation of such a shock on the trailing edge of a compression wave at $T > T_\alpha$ (or at the front of a rarefaction wave for $\delta T < 0$) is a specific property of second sound in He-II[23,24,14]. At small $W < 0.7$ W/cm^2 the bolometer detected linear waves (curves 1,2) of amplitude δT_2 proportional to W. Above $W = 1$ W/cm^2 and up to 17 W/cm^2 the pulse shape is nearly triangular (linear waves transforming to planar shock waves, curves 3–5). The amplitude of the triangular pulse δT_2 and its width

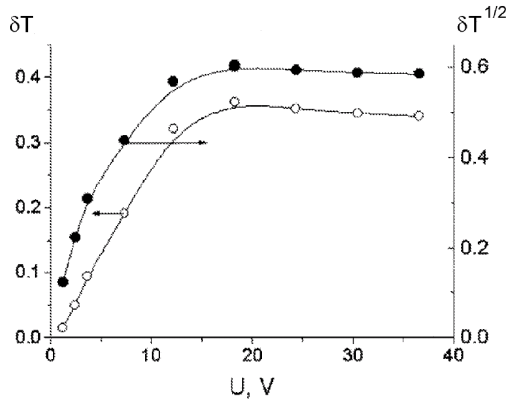

Fig. 3 Dependence of the amplitude of second sound wave $\delta T(U)$ on the pulsed voltage U to the heater, reconstructed from Fig. 2(a) (left-side scale, open circles), and the dependence on $\delta T^{1/2}$ on U (right-side scale, solid circles). Arrows indicate the relevant ordinate scales. From Efimov et al[26]

increase proportional to $W^{1/2}$. Above 30 W/cm^2 (curves 6 and 7) the amplitude and the width of the pulse depend only weakly on U (the saturation regime).

Fig. 2(b) shows an equivalent set of data for $T = 1.50$ K ($\alpha > 0$) under SVP, $P = P_{\rm SVP}$, while the heat flux density increases from $W = 2.4$ W/cm^2 to 20.2 W/cm^2, at a constant distance $L = 2.5$ cm from the heater[38]. The heater pulse duration was $\tau_e = 10\ \mu$s. We see that the slope of profile $a = \delta T/\tau$ (where τ is the time duration of the broadened pulse) does not depend on W, in accordance with the general theory[13].

We restrict our discussion to the propagation of second sound pulses of relatively small amplitude $|\delta T| < 10^{-2}$ K, so that we can neglect possible complications due to creation of quantum vortices at the shock front. For small amplitude, the description of the nonlinear evolution of the second sound wave can be confined to the first term in the expansion of the velocity u_2 in δT_2, as in Eq. (1). Under this approximation the amplitude of a second sound pulse at small W (linear wave) should be proportional to W, i.e. $\delta T \propto W \propto U^2$. At higher W, where a shock wave is formed, the amplitude of the propagating triangular pulse should be $\delta T \propto W^{1/2} \propto U$.[13,26]

The experimental dependence of the amplitude of the pulse plotted as $\delta T(U)$ (left side scale, open circles) and $\delta T^{1/2}(U)$ (right-side scale, solid circles) presented in Fig. 3 was reconstructed from the measurements shown in Fig 2(a) ($T = 2.10$ K, $P = 3$ atm, and heater pulse duration $\tau_e = 10\ \mu$s).[39]

At high W the amplitude of second sound pulses saturates, as can be seen from Figs. 2 and 3. A similar dependence was observed at $P = 3$ atm and $T = 1.7$ K, where the nonlinearity coefficient $\alpha > 0$. All the curves $\delta T(U)$ obtained at different pressures and temperatures in our studies look much the same. Similar saturation effects at high W were reported in Refs.[40,41]. As will become clear below, one of the reasons for the saturation of $\delta T(U)$ lies in a nonlinear transfer of acoustic energy from the low-frequency spectral domain (positioned at frequen-

cies $\sim 1/\tau$) to high frequency spectral domain at $\omega \sim u_{20}/l_f$ (where l_f is the shock front width), i.e. the same reason that leads to the acoustic turbulence of second sound waves in He II, as discussed below.

4 ACOUSTIC TURBULENCE OF SECOND SOUND WAVES IN He II

We now consider the recent measurements[12,28,42,43] of second sound standing waves in a resonant cavity that have demonstrated the occurrence of both forward and inverse energy cascades in acoustic WT. Again, we restrict the discussion to the range of heat fluxes $W \leq 50\,\mathrm{mW\,cm^{-2}}$ for which we can neglect possible formation of quantized vortices.

4.1 Observation of a direct Kolmogorov-like cascade

Fig. 4 shows the evolution of the second sound wave spectrum with increasing AC heat flux density W from the heater, measured near 2.08 K when driving at the frequency of the 31st resonance.[12] For small $W \leq 4$ mW/cm^2 we observed a nearly linear regime of wave generation, where a small number of harmonics of the driving frequency were excited due to nonlinearity (see Fig. 4(a)), and the shape of the recorded signal was close to sinusoidal. An increase of the excitation above 10 mW/cm^2 led to visible deformation of the signal shape and to the generation of a large number of high-frequency harmonics in the second sound wave spectrum as shown in Fig. 4(b). The dependence of wave amplitude δT on the excitation level W deviates from a linear relationship above $\delta T \sim W_d^2$ (see Fig. 1 of Efimov et al.[38]

It is evident from Fig. 4 that the main spectral peak (marked by the left arrow) lies at the driving frequency ω_d, and that high-frequency peaks appear at its harmonics $\omega_n = n \times \omega_d$ with $n = 2, 3, \ldots$. It can be seen in Fig. 4(b) that a cascade of waves is formed over the frequency range up to 80 kHz, i.e. up to a frequency 25 times higher than the driving frequency. As also shown in Fig. 4(b), the dependence of peak height on frequency may be described by a power-law-like function $\delta T_\omega = \mathrm{const} \times \omega^{-s}$ for frequencies lower than some cut-off frequency ω_b that increases with increasing W. Note there are systematic uncertainties of about $\pm 10\%$ in the values of s and ω_b extracted from plots of this kind, depending on the range of ω through which the straight line is drawn. For sufficiently high AC heat flux densities $W > 12$ mW/cm^2 (i.e. for the developed cascade), the scaling index tends towards $s \approx 1.5$.

The formation of these spectra is evidently attributable to a cascade transfer of wave energy through the frequency scales due to nonlinearity, thus establishing an energy flux in K-space directed from the driving frequency towards the high-frequency domain. In accordance with basic ideas formulated in Refs.[1,2,32] we may infer that, at relatively high driving amplitudes, we are observing acoustic turbulence formed in the system of second sound waves within the inertial (nondissipative) range of frequencies. Formation of this direct cascade is similar to creation of the Kolmogorov distribution of fluid velocity over frequency in the bulk of a classical fluid[1].

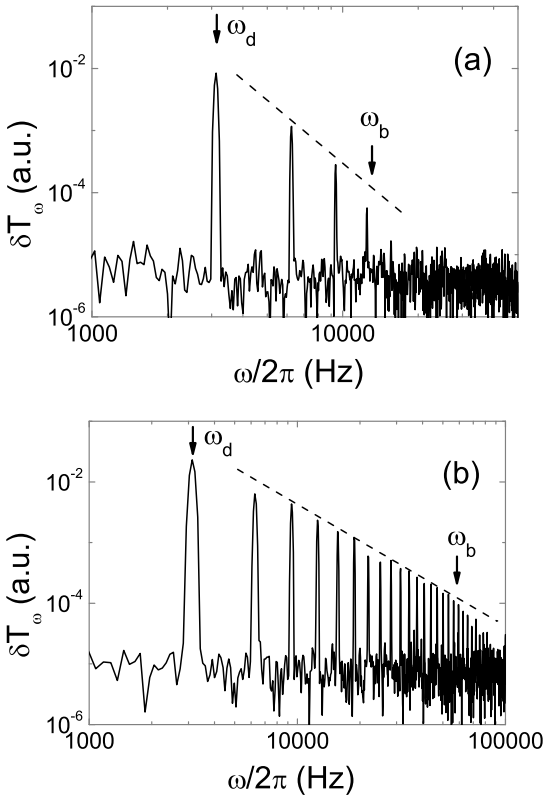

Fig. 4 Change in the power spectrum of second sound standing waves as the AC heat flux density is increased from (a) $W = 4$ mW/cm^2 to (b) 25 mW/cm^2. The system was driven at its 31st resonance, at a temperature close to 2.08 K. The dashed line in (a) is a guide to the eye, whereas that in (b) corresponds to $\delta T \propto \omega^{-1.7}$. The arrows indicate the positions of the fundamental spectral peak formed at the driving frequency ω_d and of the high-frequency edge ω_b of the inertial frequency range. From Kolmakov et al.[12]

We observed also that, when the AC heat flux density was raised above some critical value at *even* resonance numbers $p > 30$, a spectral peak appeared at the frequency equal to *half* the driving frequency (i.e. formed on the left of the fundamental peak) and at its harmonics. Fig. 5 shows the evolution of the wave spectrum with increasing AC heat flux density when driving on the 32nd resonance[44]. It is evident that, at the relatively small heat flux density of $W = 4$ mW/cm^2, the wave spectrum shown in Fig. 5(a) is quite similar to that observed under similar conditions when driving at the 31st resonance (i.e. at the nearest odd numbered resonance), cf. Fig. 4(a). Formation of the low-frequency harmonic (subharmonic) at $\omega = \omega_d/2$ at $W = 16$ mW/cm^2 is clearly evident in Fig. 5(b). It was found experimentally that the threshold for subharmonic generation with $30 < p < 96$ was about 10 mW/cm^2 (see Fig. 8 below).

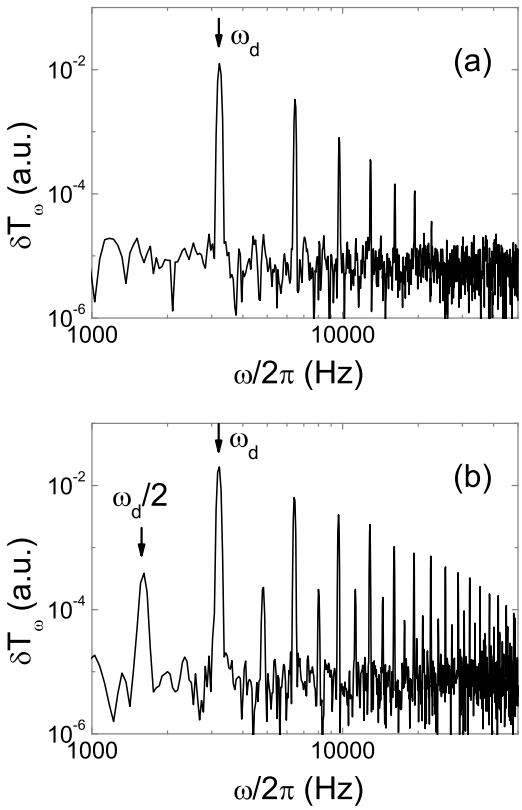

Fig. 5 Second sound wave spectra measured when driving on the frequency of the 32nd resonance with (a) $W = 4$ mW/cm^2 and (b) $W = 16$ mW/cm^2. The arrows indicate the fundamental peaks at the driving frequency $\omega = \omega_d$ and a subharmonic formed at $\omega = \omega_d/2$. The temperature was close to 2.08 K. From Ganshin et al[44]

The formation of subharmonics may be attributed to development of a decay instability of the periodic wave. In accordance with general theory[1,2,32], the instability is controlled mainly by nonlinear decay of the wave into two waves of lower frequency, and by the opposite process of the confluence of two waves to form one wave. The energy (or frequency) conservation law for this 3-wave process is given by Eq. (2). The case shown in Fig. 5(b) evidently corresponds to generation of subharmonics with $\omega_2 = \omega_3 = \omega_d/2$.

We also observed the high-frequency cutoff of the wave spectrum due to viscosity. As shown in Fig. 4(a), it manifests itself as an abrupt decrease in the amplitudes of the harmonics at $W < 10$ mW/cm^2, and as a change in slope of the spectrum at higher W (Fig. 4(b)) when plotted on double-log scales, which occurs at some characteristic frequency ω_b. At $\omega \sim \omega_b$ the nonlinear mechanism for nearly nondissipative transfer of the wave energy changes to viscous damping of the waves (cf. observations of the high-frequency edge of the inertial range of

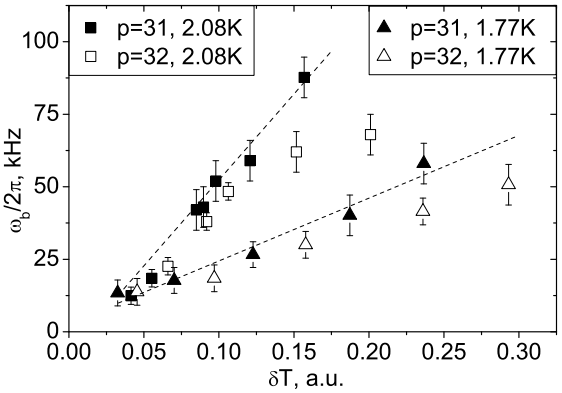

Fig. 6 Dependence of the viscous cutoff frequency $\omega_b/2\pi$ on the amplitude δT of the standing wave for different temperatures T and resonance numbers p. Dashed lines indicate the results of our numerical computations; data points represent experimental measurements. From Kolmakov et al [12]

frequencies of capillary turbulence on the surface of liquid hydrogen [45]). It causes a faster reduction of sound amplitude at frequencies $\omega > \omega_b$, as observed.

The measured dependence [12] of the boundary frequency $\omega_b/2\pi$ on the standing wave amplitude δT is shown in Fig. 6. It can be seen that the inertial range is extended towards higher frequencies when the driving force is increased. When driving at resonant frequencies with odd resonance numbers p, with sufficiently large driving amplitudes, the boundary frequency depends near linearly on wave amplitude

$$\omega_b/2\pi \approx \text{const}(T, \omega_d) \times \delta T,$$

(the filled symbols in Fig. 6). Our numerical calculations [12] are in agreement with this result.

When driving at even p (open symbols in Fig. 6) the boundary frequency is noticeably lower than that measured for the nearest odd resonance number, with $W > 10$ mW/cm^2. This reduction may be connected to a change in the mechanism of energy relaxation in the wave system caused by the generation of subharmonics with frequencies lower than ω_d.

One can see from Fig. 6 that the energy balance in the wave system is highly nonlocal in K space: energy is pumped into the system in the low-frequency (long-wave) domain and it flows to the high frequency (short-wave) domain where it is absorbed by dissipative mechanisms.

4.2 Inverse Energy Cascade of Acoustic Turbulence

It was found that, when driving at sufficiently high AC heat flux densities $W > 10$ mW/cm^2 and at resonance numbers $p > 50$, multiple subharmonics were generated in the low-frequency spectral domain $\omega < \omega_d$. Fig. 7 presents typical results

obtained when driving at a relatively high resonant frequency ω_d (the 96th longitudinal resonance of the cell). Those in Figs. 7(a),(b) reproduce our earlier observation of the direct Kolmogorov-like cascade of second sound waves in He II [12], when driving close to resonance. Figs. 7(c)–(f) show the evolution of the wave shape and spectrum with changes in the detuning of the drive frequency up to $\Delta = (\omega_d - \omega_p)/\omega_p = 5 \times 10^{-4}$. Of particular interest for what follows, tiny shifts in driving frequency result in marked changes in the shape and power spectrum of the standing wave. The formation of spectral peaks near $\frac{1}{2}$, $\frac{1}{3}$ and $\frac{2}{3} \times \omega_d$ satisfy (2) with $\omega_1 = \omega_d$, supporting our inference that the instability is controlled mainly by 3-wave interactions. We comment that the subharmonic generation giving rise to the inverse cascade bears striking similarities to the Feigenbaum period-doubling route to chaos [46]. Huge distortions of an initially periodic signal occur as the driving frequency changes, as shown in Fig. 7(c),(e): when the instability develops, the signal remains nearly periodic, but its characteristic period becomes considerably longer than the fundamental period of the driving force (shown by horizontal arrows in the left-hand column of Fig. 7). The amplitude of the lower-frequency waves can reach more than twice that at the driving frequency.

We can use the energy contained in the low-frequency part of the spectrum $\omega < \omega_d$,

$$E_{LF} = \frac{1}{2}\left(\frac{\partial C}{\partial T}\right) \sum_{\omega<\omega_d} |\delta T_\omega|^2, \tag{4}$$

as an indicator to characterise the instability quantitatively. For small W we did not observe any subharmonic generation at all [12]; then, above a critical flux W_c, E_{LF} rose rapidly [28], as shown in Fig. 8, suggesting that the phenomenon is of a threshold character. At $T = T_\alpha = 1.88$ K for which α vanishes [22], no subharmonics were observed, regardless of the magnitude of W, thus confirming the crucial importance of nonlinearity. For W above 10.4 mW/cm^2, we observed a distortion of the signal similar to that shown in Fig. 7(c) and the formation of a few subharmonics. Further increase of W above 20 mW/cm^2 led to the generation of multiple subharmonics. These phenomena appear in the regime where the energy cascade towards the high frequency domain (i.e. direct cascade, with a Kolmogorov-like spectrum [12,47]), is already well-developed.

4.3 Combinational frequencies and spectrum suppression

It is also of interest to study the response to a driving waveform more complex than the simple sinusoid discussed above. We have therefore investigated the result of applying a weak secondary drive at a different frequency, in addition to the main driving force. The result [42] is a marked decrease in the energy at high frequencies. It seems that this effect can arise in two ways. One of these is that the turbulent energy travels faster and more easily towards the high frequency domain where dissipation occurs. Secondly, and in addition, under appropriate conditions the additional drive triggers the onset of the inverse cascade. An example is shown in Fig. 9: two harmonic voltage generators were used, one providing the main drive of $W = 21.5$ mW/cm^2 on the 40th resonance, $\omega_{d1}/2\pi = 4020.6$ Hz, producing a developed direct energy cascade; the other applied the perturbing force of $W = 3.4$ mW/cm^2 on the 9th resonance, $\omega_{d2}/2\pi = 858.3$ Hz.

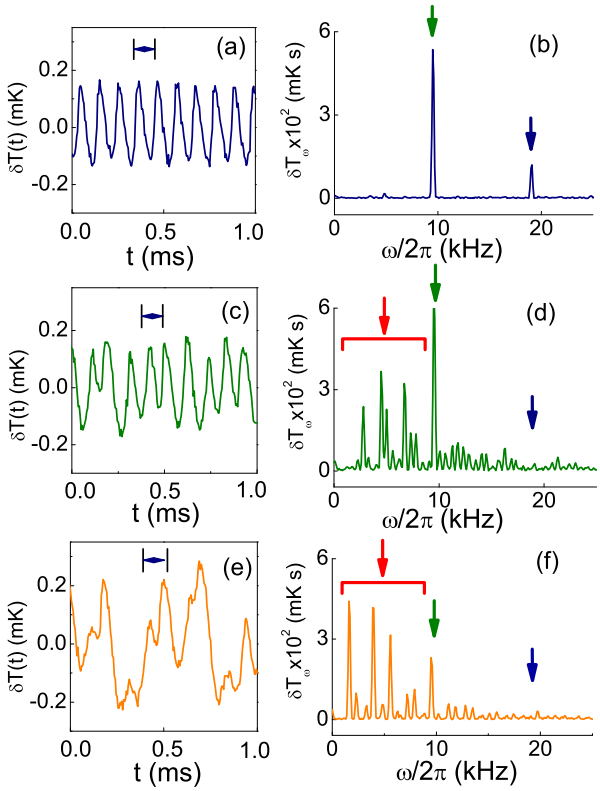

Fig. 7 Evolution of the observed wave shape in the resonator in a steady state (left column) and of the power spectrum of second sound standing waves (right) with increasing (small) positive detuning of the drive frequency ω_d near the 96th resonance: (a),(b) $\omega_d/2\pi = 9530.8$ Hz; (c),(d) 9532.4 Hz; and (e),(f) 9535.2 Hz. The AC heat flux density was $W = 42$ mW/cm^2. The temperature $T = 2.08$ K corresponded to negative nonlinearity. The fundamental and first harmonic in (b),(d),(f) are indicated by vertical (green and blue) arrows; the low-frequency domain where the subharmonics appear are indicated by the horizontal ranges in (d),(f) with vertical (red) arrows. The horizontal arrows in (a),(c),(e) indicate the fundamental period of a wave at the driving frequency. From Efimov et al.[43]

It is clearly seen that additional peaks are formed at *combination* frequencies $\omega_{mn} = m \times \omega_{d1} + n \times \omega_{d2}$ (where n and m are integer numbers) along with harmonics of the main driving frequency. These peaks are evidently formed through nonlinear interactions between the waves at the main and additional driving frequencies. This phenomenon is similar to the generation of combination frequencies during the propagation of light through a nonlinear optical medium[48]. Formation of Stokes and anti-Stokes satellites of the 2nd harmonics of the main drive at frequencies $\omega = 2\omega_{d1} \pm \omega_{d2}$, corresponding to "absorption" and "emission" of the second sound waves with frequency ω_{d2} due to nonlinearity, is clearly seen in the spectrum shown in the inset of Fig. 9.

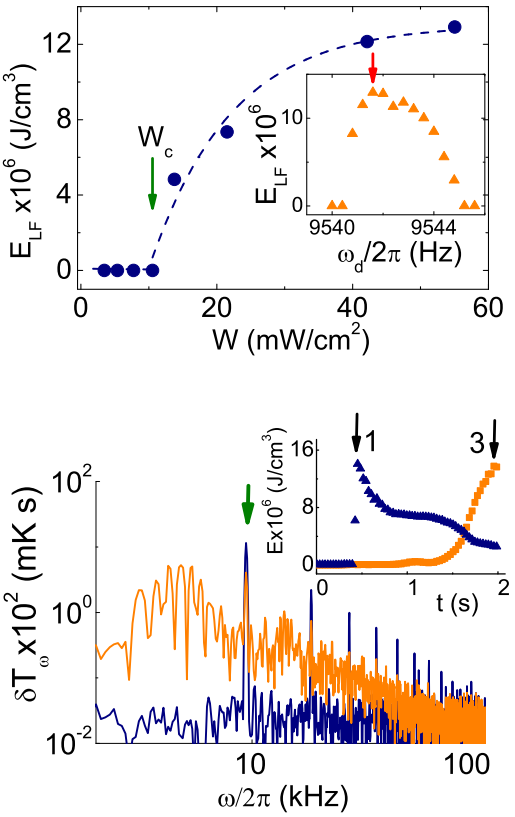

Fig. 8 **Top**: The energy E_{LF} contained in the low-frequency part of the steady-state spectrum as a function of the AC heat flux density W, while driving near to the 96th resonance for $T \simeq 2.08$ K. The threshold value of W, marked by the (green) arrow, was $W_c = 10.4$ mW/cm^2. The points are from experiment; the dashed line is a guide to the eye. Inset: the dependence of E_{LF} on ω_d, measured for $W = 55.6$ mW/cm^2; the (red) arrow labels the maximum value of E_{LF}, which is taken to the main figure. **Bottom**: Instantaneous spectra in frames 1 and 3 of Fig. 10. The lower (blue) spectrum, for frame 1, shows the direct cascade only; the upper (orange) spectrum, for frame 3, shows both the direct and inverse cascades. The (green) arrow indicates the the fundamental peak at the driving frequency. Inset: evolution of the wave energy in the low-frequency and high frequency domains is shown by the (orange) squares and (blue) triangles respectively; (black) arrows mark the positions of frames 1 and 3. From Ganshin et al[28]

4.4 Transient processes

The above results all correspond to steady-state regimes of the wave system. In Figs. 8 (bottom) and 10 we illustrate the *transient* processes observed after a step-like shift of the driving frequency from a frequency initially set far from any resonance to the 96th resonance frequency for $W = 42.1$ mW/cm^2, $T = 2.08$ K. We find that harmonics of the drive in the high-frequency spectral domain are formed very quickly, but that formation of the subharmonics takes much longer: it took ~ 0.5 s here, and can reach several tens of seconds under some conditions[28]. It is evident from the inset in Fig. 10 that, as the instability develops, isolated "rogue

waves" appear in the signal. As time evolves, the rogue waves appear more frequently and, in the later stages, they merge resulting in the strong low-frequency modulation of the signal observed in the steady-state measurements (Fig. 7).

When the subharmonics appear, a marked reduction occurs in the energy contained in the high-frequency spectral domain[28]. Much of the energy injected at the driving frequency ω_d then flows towards the low frequency domain $\omega < \omega_d$ leading to an accumulation of wave energy there, with a corresponding increase in wave amplitude. The reduction of wave amplitude seen in the high frequency spectral domain clearly indicates the onset of energy backflow towards lower frequencies, i.e. a sharing of the flux between the direct and inverse energy cascades. The decrease in energy at high frequencies in the interval $0.397s < t < 1.3$ s is attributable to relaxation processes in the direct cascade. The corresponding redistribution of wave energy between the direct and inverse cascades starts at about $t = 1.3$ s. The transient evolution shown in Figs. 8 (bottom) and 10 is incomplete: the forward and inverse energy fluxes are still changing at $t = 2s$, implying further relaxation oscillations at longer times (inaccessible with our present equipment): the transient dynamics is highly complex, and a full characterisation will require further work. For there to be a flux of energy towards low frequencies, there must of course be some dissipative mechanism there. We believe that it is probably attributable to viscous drag of the normal fluid component on the resonator walls, given that bulk second sound damping is negligibly small in this frequency range[49]: this would be consistent with the observed strong decrease of

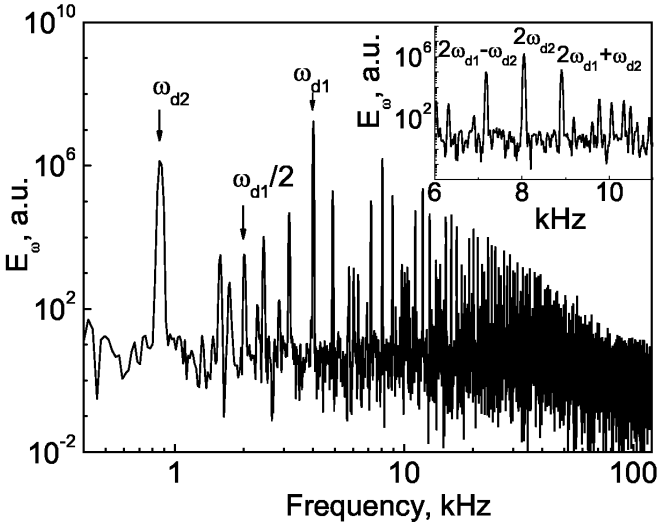

Fig. 9 Energy spectrum of standing second sound waves measured at $T = 2.08$ K when driving simultaneously at two frequencies of the 9th and 40th resonances. The main driving frequency is $\omega_{d1}/2\pi = 4020.6$ Hz, the additional driving frequency is $\omega_{d2}/2\pi = 858.3$ Hz. The inset shows an enlarged part of the spectrum near the 2nd harmonic of ω_{d1} in semi-log scale. From McClintock et al.[42]

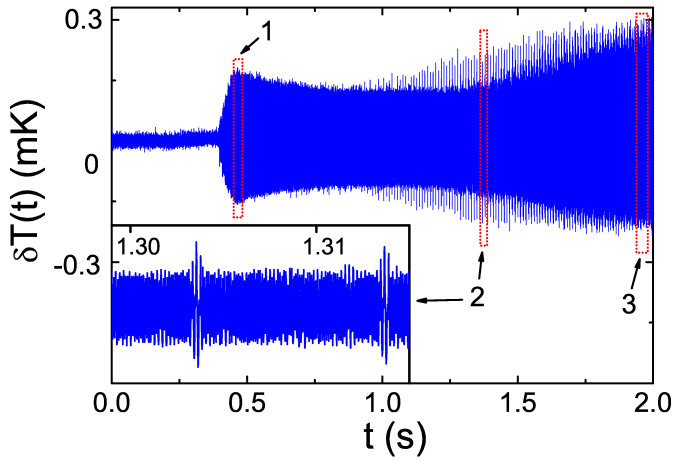

Fig. 10 Transient evolution of the 2nd sound wave amplitude δT after a step-like shift of the driving frequency to the 96th resonance at time $t = 0.397$ s. The AC heat flux density was $W = 42.1$ mW/cm^2, the temperature was $T = 2.08$ K. Signals in frames 1 and 3 are similar to those obtained in steady-state measurements, Fig. 7(a) and (e) respectively. Formation of isolated "rogue" waves are clearly evident. Inset: examples of isolated rogue waves, enlarged from frame 2. From Ganshin et al.[28]

the resonator Q-factor below 3 kHz. There is *hysteresis* between increasing and decreasing frequency scans (bars on data points in Fig. 13). The width of the hysteretic region, i.e. the region where the low frequency sound waves are metastable, was less than the viscous width of the resonance.

4.5 Probability distributions of the higher harmonics

It is of interest to explore how the coherence of the driving force diminishes as the energy moves towards the higher harmonics. We have investigated[50] this question through analysis of a developed acoustic cascade at $T = 2.08$ K. The system was driven at the 51st resonance, $\omega_d/2\pi = 5030$ Hz, with $W = 25$ mW/cm^2. We used a digital filter to eliminate selected numbers of lower harmonics and computed the probability distribution function (PDF) of the rest of the signal. The resultant changes in the PDF are shown in Fig. 11.

It is evident that, as expected, the main harmonic is defined by the resonant driving signal and corresponds to a strongly distorted sine wave: its PDF is very similar to that of a sine wave. The driving signal also influences directly the next few harmonics, but fades out for the higher ones, which become more Gaussian-like. The intensity of noise in the measurement system was an order of magnitude less than the random fluctuations in the second sound intensity. Some asymmetry was visible, however, in all measurements as shown in the figure. It originates in the non-sinusoidal shape of the recorded signals: the heating peak is accom-

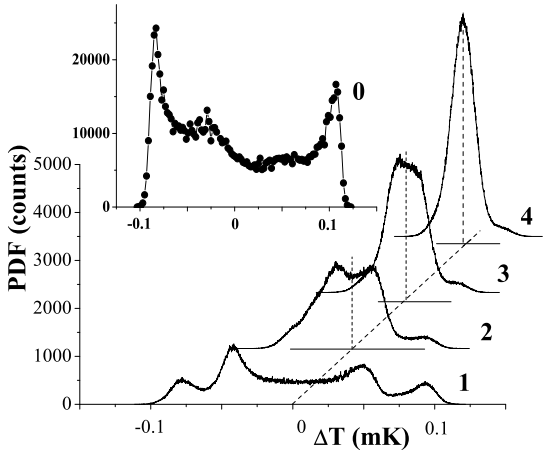

Fig. 11 Evolution of the PDF of a second sound standing wave during sequential removal of its lower frequency harmonics. The number beside each PDF shows the lowest order harmonic that is retained (so that 0 indicates the PDF of the full original signal, 1 indicates retention of 1st and higher harmonics after removal of the fundamental, and so on). From Efimov et al.[50]

panied by distinctive breakdowns at the front or tail, depending on the sign of the nonlinear coefficient α. Comparable asymmetry was observed for first sound resonances in closed tubes[51], as well as for heating and cooling shock waves in superfluid helium[38] and measurements of the PDF of capillary surface waves[52,53]. In the present case, because the minima in δT are more rounded than the maxima, there is a corresponding asymmetry in the PDF. It decreases for the higher harmonics but does not completely disappear within the experimentally accessible range.

Substantial phase-mixing in the higher frequency modes is probably caused by weak four-wave interaction (i.e. by a higher-order nonlinear process). As a result, their relative phases will be less affected by the phase of the driving force. Hence the PDFs of the higher harmonics become nearly Gaussian, as observed, apparently corresponding to chaotic-like behavior.

5 NUMERICAL SIMULATIONS AND DISCUSSION

We have applied a numerical technique to gain a more detailed understanding of wave energy transformation in the acoustic turbulence regime[28]. It involves direct integration of the 2-fluid thermohydrodynamical equations[13], expanded up to quadratic terms in the wave amplitude. It represents the second sound waves in terms of Hamiltonian variables[12,54], similar to the approach used in earlier studies[47] of acoustic turbulence. Wave damping was taken explicitly into account at all frequencies, however, a feature that is of key importance for a correct description of subharmonic generation. To correspond with the experimental conditions,

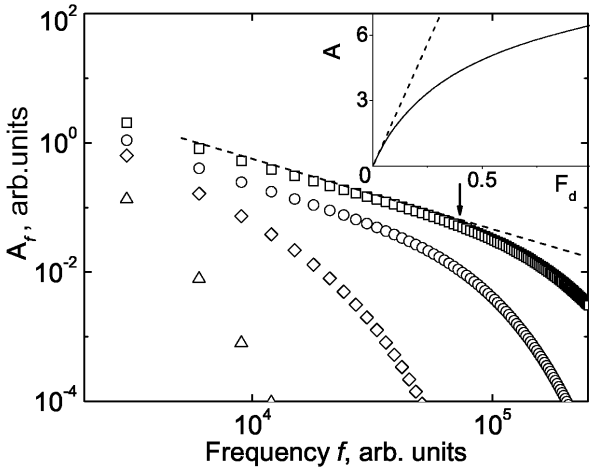

Fig. 12 Second-sound power spectral amplitude A_f calculated numerically for four different driving force amplitudes below a critical amplitude for the low-frequency instability: $F_d = 0.01$ (triangles), 0.05 (diamonds), 0.1 (circles), and 0.3 (squares). The dashed line corresponds to $A_f \propto f^{-1}$. The arrow marks the boundary frequency of the inertial interval for $F_d = 0.3$. The inset shows the calculated dependence on F_d of the standing wave amplitude A: solid line, nonlinear waves, $\alpha < 0$ ($T > T_\alpha$); dashed line, linear waves, $\alpha = 0$ ($T = T_\alpha$). From Kolmakov et al.[12]

we assume full reflection of the waves from the resonator boundaries, rather than periodic boundary conditions[47]. *We also suppose in computations that the spectrum of resonant frequencies is equidistant and the dispersion law for the second sound waves is a purely linear function.*

Fig. 12 shows the evolution of the steady-state spectrum with increasing driving force amplitude F_d, calculated[12] for $\alpha < 0$ ($T > T_\alpha$). Points on the plot correspond to the amplitudes of the peaks in the spectrum. It is seen that, at small driving amplitude $F_d \sim 0.01$ (triangles), viscous damping prevails at all frequencies and a turbulent cascade is not formed: the amplitude of the second harmonic is an order of magnitude less that that of the fundamental. In this regime the wave shape is close to linear. At intermediate driving amplitude $F_d \sim 0.05$ (diamonds) nonlinearity starts to play a role at frequencies of the order of driving frequency, and a few harmonics are generated (cf. Fig. 4(a)). At high driving amplitudes $F_d \geq 0.1$ (circles and squares) a well-developed cascade of second sound waves is formed up to frequencies 30 times higher than the driving frequency, i.e. the behaviour predicted by the computations is very similar to that observed in our experiments (Fig. 4.(b)). From the calculated dependence on F_d of the standing wave amplitude (Fig. 12, inset) we can conclude that the deviations from the linear dependence $A \propto F_d \propto W$ (where W is the oscillating component of the emitted heat flux) observed at small driving amplitudes are caused by nonlinear outflow of the energy to higher frequency scales.

In some range of frequencies the calculated spectrum obeys a power law with $s \approx 1$ (squares in Fig. 12). This observation is in qualitative agreement with the theory[55], where a similar spectrum was obtained as the Fourier-transform of a set of traveling shock waves. The difference in slope of the calculated spectrum from

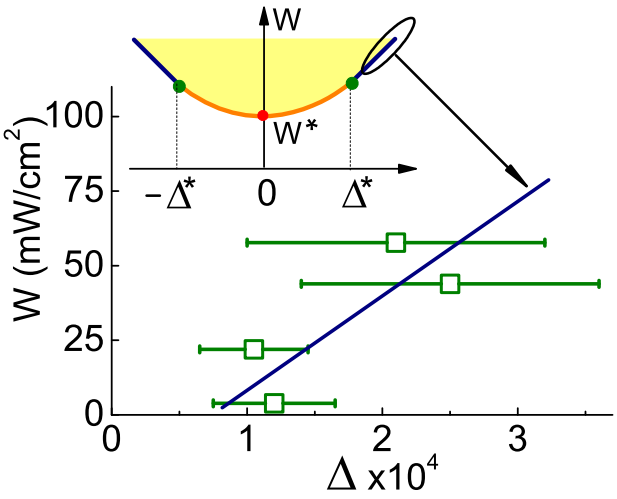

Fig. 13 Dependence of the AC heat flux density W at which the instability develops on the dimensionless frequency detuning $\Delta = (\omega_d - \omega_p)/\omega_p$ of the driving force frequency ω_d from a cavity resonance ω_p. Numerical calculations (line) are compared with measurements (points) for driving at the 96th resonance. Horizontal bars mark the widths of the hysteretic region where second sound exists in a metastable state. Inset: bifurcation diagram showing regions of stability (unshaded) and regions of instability (yellow shaded) against the generation of subharmonics. The soft instability occurs over the (orange) line between the (green) critical points at $\pm\Delta^*$; outside them lies the hard instability; W^* is the threshold value of the instability. From Ganshin et al.[28]

the value $s \approx 1.5$ observed in the experiment may be attributable to our resonator having an insufficiently high quality factor, as well as to the influence of other mechanisms of wave energy relaxation not taken into account in our computations. Also, the difference may be caused[56] by changes in the statistical properties of the harmonics, from being coherent (at relatively low frequencies) to having random phase distributions (at high frequencies), as demonstrated in Fig. 11. The precise identification of the scaling index characterising a turbulent distribution is obviously important for connecting the theory to real physical experiments. To clarify the origin of the difference between observations and computations, one needs to make further measurements and to undertake a systematic study in the vicinity of T_λ, where the nonlinearity of second sound rises much faster than its damping[57], and the proper Mach and Reynolds numbers should therefore be substantially increased.

We also found that, for sufficiently high driving amplitude W, the wave develops an instability with respect to generation of low-frequency subharmonics of the driving force at ω_d: see inset of Fig. 13. For zero detuning from a cavity resonance, the onset of the instability occurs at a threshold $W^* \propto 1/|\alpha|$. If the dimensionless frequency detuning $|\Delta|$ is less than a critical value $\Delta^* \sim 1/Q$, the instability has a soft character, in that the amplitudes of the low frequency waves tend to zero at the threshold bifurcation line. Outside this range, the low frequency waves are characterised by the hard onset observed experimentally. Measurements (squares)

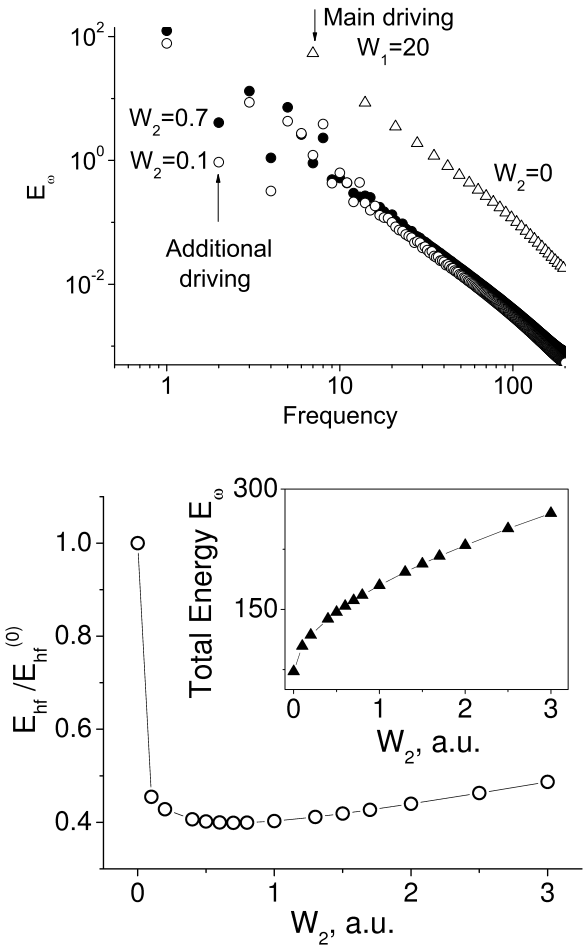

Fig. 14 Effect of a weak secondary forcing. The upper panel plots the stationary power spectra for different amplitudes of the secondary drive: $W_2 = 0$ (triangles); and nonzero W_2 (filled and open circles). The lower panel plots the energy in the high frequency domain (arbitrary units) as a function of W_2. From Efimov et al.[43]

are compared with theory (full line) in the main part of Fig. 13. The hard onset is accompanied by a finite jump in subharmonic amplitude. These two regimes of behaviour are separated by critical points on the bifurcation line. The generation of subharmonics in the nonlinear oscillatory system found numerically appears to be similar to the bifurcation of an anharmonic oscillator[58]. The estimated value of the critical detuning parameter Δ^* at $T = 2.08$ K is close to 10^{-4}, and that of the critical AC heat flux density W^* is equal to a few mW/cm^2, in good agreement with the observations. The results of Fig. 7 can be understood as corresponding to the working point moving horizontally on the bifurcation diagram (Fig. 13, inset) into the (yellow) shaded region from a position just outside it, through the

hard (blue) instability line. Nonlocal (in ω-space) interactions between waves at ω_d and low frequency waves probably contribute to the subharmonics, due to the finite width of the low-frequency spectral domain, but we estimate that the interactions of high-frequency ($\omega \gg \omega_d$) waves with subharmonics are relatively weak, consistent with our inference of two distinct cascades.

The numerical calculations can also encompass the main effects of double-driving. Fig. 14 illustrates the calculated effect of applying a weak additional driving force. The upper panel shows how the spectra are modified by application of a lower-frequency secondary forcing at amplitudes W_2 that are 10% and 70% of the main drive. There is a marked decrease in the energy flux to the high frequency domain. The effect is quite insensitive to the amplitude of the secondary drive. These dramatic changes are shown explicitly in the lower panel. At the same time, the total turbulent wave energy increases monotonically with W_2. It is evident (upper panel) that the secondary forcing has triggered the inverse cascade, causing the onset of an energy flux towards the low-frequency domain.

A physically intuitive explanation of these phenomena is that the additional forcing effectively relaxes the conservation laws governing the nonlinear wave transformations, and thus opens up many more channels via which the frequency-changing interactions can occur.

6 CONCLUSIONS

The experiments described above have revealed direct and inverse wave energy cascades in a turbulent acoustic system. The inverse cascade is responsible for a substantial increase in wave amplitude and for the formation of high-amplitude, low-frequency, subharmonics. The instability develops through formation of isolated low-frequency waves of higher amplitude than is typical of the waves around them. These higher-amplitude lone waves can be considered as the acoustic analogue of the giant "rogue" waves that occasionally appear on the ocean and endanger shipping. Their origin lies in a decay instability of the periodic wave, i.e. a similar mechanism to that proposed[59,29] (modulation instability) to account for the creation of oceanic rogue waves[60]. We have also glimpsed a rich manifold of kinetic phenomena waiting to be explored in future experimental and theoretical investigations.

Finally, we emphasise that these studies of wave turbulence are likely to impact on the several other areas of physics mentioned in Sec. 1. Practical applications can readily be envisaged in relation to the extraction of energy from ocean waves, where we have the possibility of using tailored perturbations to alter the dominant wavelength to match the optimal characteristics of the machinery in use. It is also possible that an improved understanding of how "rogue" waves originate may eventually lead to methods for predicting or attenuating them.

Acknowledgements We are grateful to V. E. Zakharov, E. A. Kuznetsov, A. A. Levchenko and M. Yu. Brazhnikov for valuable discussions. The investigations were supported by the Russian Foundation for Basic Research project Nos. 07-02-00728 and 06-02-17253, by the Presidium of the Russian Academy of Sciences in framework of the programmes "Quantum Macrophysics" and "Mathematical Methods in Nonlinear Dynamics", by the Royal Society of London, and by the Engineering and Physical Sciences Research Council (U.K.).

References

1. A. N. Kolmogorov, *Doklady Akad. Nauk S.S.S.R.* **30**, 299 (1941).
2. V. E. Zakharov, V. S. L'vov, and G. Falkovich, *Kolmogorov Spectra of Turbulence I* (Springer, Berlin, 1992).
3. U. Frisch, *Turbulence* (Cambridge University Press, Cambridge, 1995).
4. P. A. Davidson, *Turbulence: An Introduction for Scientists and Engineers* (Oxford University Press, Oxford, 2004).
5. F. P. Incropera and D. P. DeWitt, *Fundamentals of Heat Transfer* (Wiley, New York, 1981).
6. W. F. Vinen and J. J. Niemela, *J. Low Temp. Phys.* **128**, 167 (2002).
7. W. F. Vinen, *J. Low Temp. Phys.* **145**, 7 (2006).
8. V. S. Tsoi, *CEJP* **1**, 72 (2003).
9. S. N. Gurbatov, V. V. Kurin, L. M. Kustov, and N. V. Pronchatov-Rubtsov, *Acoust. Phys.* **51**, 152 (2005).
10. G. S. Bisnovatyi-Kogan and S. A. Silich, *Rev. Mod. Phys.* **67**, 661 (1995).
11. M. Ryutova and T. Tarbell, *Phys. Rev. Lett.* **90**, 191101 (2003).
12. G. V. Kolmakov, V. B. Efimov, A. N. Ganshin, P. V. E. McClintock, and L. P. Mezhov-Deglin, *Phys. Rev. Lett.* **97**, 155301 (2006).
13. L. D. Landau and E. M. Lifshitz, *Fluid Mechanics* (Butterworth and Heinemann, Oxford, 1987).
14. I. M. Khalatnikov, *An Introduction to the Theory of Superfluidity* (Benjamin, New York, 1965).
15. C. C. Ackerman, B. Bertman, H. A. Fairbank, and R. A. Guyer, *Phys. Rev. Lett.* **16**, 789 (1966).
16. S. J. Putterman, *Superfluid Hydrodynamics* (North-Holland, Amsterdam, 1974).
17. A. Y. Iznankin and L. P. Mezhov-Deglin, *Sov. Phys. JETP* **57**, 801 (1983).
18. I. Y. Borisenko, V. B. Efimov, and L. P. Mezhov-Deglin, *Sov. J. Low Temp. Phys.* **14**, 619 (1988).
19. L. P. Mezhov-Deglin, A. Y. Iznankin, and V. P. Mineev, *JETP Lett.* **32**, 199 (1980).
20. L. S. Goldner, G. Ahlers, and R. Mehrotra, *Phys. Rev. B* **43**, 12861 (1991).
21. S. K. Nemirovskii, *Soviet Phys. Usp.* **33**, 429 (1990).
22. A. J. Dessler and W. H. Fairbank, *Phys. Rev.* **104**, 6 (1956).
23. H. N. V. Temperley, *Proc. Phys. Soc. (Lond.) A* **64**, 105 (1951).
24. D. V. Osborne, *Proc. Phys. Soc. (Lond.) A* **64**, 114 (1951).
25. R. J. Atkin and N. Fox, *J. Phys. C: Solid St. Phys.* **18**, 1585 (1985).
26. V. B. Efimov, G. V. Kolmakov, E. V. Lebedeva, L. P. Mezhov-Deglin, and A. B. Trusov, *J. Low Temperature Phys.* **119**, 309 (2000).
27. J. A. Tyson and D. H. Douglass, Jr., *Phys. Rev. Lett.* **21**, 1308 (1968).
28. A. N. Ganshin, V. B. Efimov, G. V. Kolmakov, L. P. Mezhov-Deglin, and P. V. E. McClintock, *Phys. Rev. Lett.* **101**, 065303 (2008).
29. A. I. Dyachenko and V. E. Zakharov, *JETP Lett.* **81**, 255 (2005).
30. D. R. Solli, C. Ropers, P. Koonath, and B. Jalali, *Nature* **450**, 1054 (2007).
31. P. W. Anderson and H. Suhl, *Phys. Rev.* **100**, 1788 (1955).
32. V. S. L'vov, *Wave Turbulence under Parametric Excitation. Application to Magnetics* (Springer, Berlin, 1994).

33. T. Matsushita, R. Nomura, H. H. Hensley, H. Shiga, and T. Mizusaki, *J. Low Temp. Phys.* **105**, 67 (1996).
34. S. R. Spangler, J. A. Leckband, and I. H. Cairns, *Phys. Plasmas* **4**, 846 (1997).
35. D. Rinberg, V. Cherepanov, and V. Steinberg, *Phys. Rev. Lett.* **76**, 2105 (1996).
36. V. B. Efimov, A. N. Ganshin, P. V. E. McClintock, G. V. Kolmakov, and L. P. Mezhov-Deglin, *J. Low Temp. Phys.* **145**, 155 (2006).
37. H. Davidowitz, Y. Lvov, and V. Steinberg, *Physica D* **84**, 635 (1995).
38. V. B. Efimov, G. V. Kolmakov, A. S. Kuliev, and L. P. Mezhov-Deglin, *Low Temp Phys.* **24**, 81 (1998).
39. I. Y. Borisenko, L. P. Mezhov-Deglin, and V. Z. Rozenflantz, *Prib. Tekh. Exp.* **5**, 137 (1987).
40. L. S. Goldner, N. Mulders, and G. Ahlers, *J. Low Temp. Phys.* **93**, 131 (1993).
41. A. Ganshin and N. Mulders, *Phys. Rev. B* **69**, 172502 (2004).
42. P. V. E. McCintock, V. B. Efimov, A. N. Ganshin, G. V. Kolmakov, and L. P. Mezhov-Deglin, *J. Low Temp. Phys.* **150**, 394 (2008).
43. V. B. Efimov, A. N. Ganshin, G. V. Kolmakov, P. V. E. McClintock, and L. P. Mezhov-Deglin, in M. Robnik and V. Romanovski, eds., *Let's Face Chaos Through Nonlinear Dynamics,* Proc. of 7th Intern. Summer School and Conf. in Maribor, volume 1076, pp. 53–62 (AIP Conf. Proc., Melville, NY, 2008).
44. A. N. Ganshin, P. V. E. McClintock, V. B. Efimov, G. V. Kolmakov, and L. P. Mezhov-Deglin, *Low Temp. Phys.* **34**, 288 (2008).
45. G. V. Kolmakov, M. Y. Brazhnikov, A. A. Levchenko, A. V. Abdurakhimov, P. V. E. McClintock, and L. P. Mezhov-Deglin, in W. P. Halperin and M. Tsubota, eds., *Progress in Low Temperature Physics: Quantum Turbulence*, volume 16, pp. 303–349 (Elsevier, Amsterdam, 2009).
46. R. L. Devaney, *An Introduction to Chaotic Dynamical Systems* (Addison-Wesley, Reading, 2000).
47. G. Falkovich and M. Meyer, *Phys. Rev. E* **54**, 4431 (1996).
48. P. A. Franken, A. E. Hill, C. W. Peters, and G. Weinreich, *Phys. Rev. Lett.* **7**, 118 (1961).
49. K. N. Zinov'eva, *Sov. Phys. JETP* **4**, 36 (1957).
50. V. B. Efimov, A. N. Ganshin, and P. V. E. McClintock, *Phys. Rev. E* **78**, 066611 (2008).
51. W. Chester, *J. Fluid Mech.* **18**, 44 (1964).
52. E. Falcon, C. Laroche, and S. Fauve, *Phys. Rev. Lett.* **98**, 094503 (2007).
53. L. V. Abdurakhimov, M. Y. Brazhnikov, and A. A. Levchenko, *JETP Lett.* **88**, 19 (2008).
54. V. L. Pokrovskii and I. M. Khalatnikov, *Sov. Phys. JETP* **44**, 1036 (1976).
55. B. B. Kadomtsev and V. I. Petviashvili, *Sov. Phys. Doklady* **15**, 539 (1970).
56. V. E. Zakharov and R. Z. Sagdeev, *Doklady Akad. Nauk S.S.S.R.* **15**, 439 (1970).
57. L. S. Goldner, G. Ahlers, and R. Mehrotra, *Physica. B* **165**, 539 (1990).
58. L. Mandelstam and N. Papalexi, *Z. Phys.* **73**, 223 (1932).
59. M. Onorato, A. R. Osborne, M. Serio, and S. Bertone, *Phys. Rev. Lett.* **86**, 5831 (2001).
60. R. G. Dean, in A. Torum and O. T. Gudmestad, eds., *Water Wave Kinetics*, pp. 609–612 (Kluwer, Amsterdam, 1990).